



HAL
open science

A novel registration-based algorithm for prostate segmentation via the combination of SSM and CNN

Chunxia Qin, Puxun Tu, Xiaojun Chen, Jocelyne Troccaz

► **To cite this version:**

Chunxia Qin, Puxun Tu, Xiaojun Chen, Jocelyne Troccaz. A novel registration-based algorithm for prostate segmentation via the combination of SSM and CNN. *Medical Physics*, 2022, 49 (8), pp.5268-5282. 10.1002/mp.15698 . hal-03654900

HAL Id: hal-03654900

<https://hal.science/hal-03654900v1>

Submitted on 29 Apr 2022

HAL is a multi-disciplinary open access archive for the deposit and dissemination of scientific research documents, whether they are published or not. The documents may come from teaching and research institutions in France or abroad, or from public or private research centers.

L'archive ouverte pluridisciplinaire **HAL**, est destinée au dépôt et à la diffusion de documents scientifiques de niveau recherche, publiés ou non, émanant des établissements d'enseignement et de recherche français ou étrangers, des laboratoires publics ou privés.

A novel registration-based algorithm for prostate segmentation via the combination of SSM and CNN

Chunxia Qin^{a,b}; Puxun Tu^a; Xiaojun Chen^a; Jocelyne Troccaz^c
a. School of Mechanical Engineering, Shanghai Jiao Tong University, Shanghai, China;
b. School of Biomedical Engineering, Shanghai Jiao Tong University, Shanghai, China;
c. Univ. Grenoble Alpes, CNRS, Grenoble INP, TIMC, Grenoble, France

April 16, 2022

Chunxia Qin and Puxun Tu contributed equally to this work.

Corresponding author: Xiaojun Chen. email: xiaojunchen@sjtu.edu.cn.

Abstract

Purpose: Precise determination of target is an essential procedure in prostate interventions, such as prostate biopsy, lesion detection, and targeted therapy. However, the prostate delineation may be tough in some cases due to tissue ambiguity or lack of partial anatomical boundary. In this study, we proposed a novel supervised registration-based algorithm for precise prostate segmentation, which combine the convolutional neural network (CNN) with a statistical shape model (SSM).

Methods: The proposed network mainly consists of two branches. One called SSM-Net branch was exploited to predict the shape transform matrix, shape control parameters, and shape fine-tuning vector, for the generation of the prostate boundary. Furtherly, according to the inferred boundary, a normalized distance map was calculated as the output of SSM-Net. Another branch named ResU-Net was employed to predict a probability label map from the input images at the same time. Integrating the output of these two branches, the optimal weighted sum of the distance map and the probability map was regarded as the prostate segmentation.

Results: Two public datasets PROMISE12 and NCI-ISBI 2013 were utilized to evaluate the performance of the proposed algorithm. The results demonstrate that the segmentation algorithm achieved the best performance with an SSM of 9500 nodes, which obtained a dice of 0.907 and an average surface distance of 1.85 mm. Compared with other methods, our algorithm delineates the prostate region more accurately and efficiently. In addition, we verified the impact of model elasticity augmentation and the fine-tuning item on the network segmentation capability. As a result, both factors have improved the delineation accuracy, with dice increased by 10% and 7% respectively.

Conclusions: Our segmentation method has the potential to be an effective and robust approach for prostate segmentation.

Keywords: registration-based segmentation, statistical shape mode, probability map, boundary distance map

39 **Contents**

40 **I. Introduction** **1**

41 **II. Materials and methods** **3**

42 II.A. Statistical shape model 4

43 II.B. CNN architecture of the segmentation framework 7

44 II.C. Grid mapping 8

45 II.D. Loss function 9

46 II.E. Inference of prostate region 11

47 **III. Results** **12**

48 III.A. Data acquisition and experiment set up 12

49 III.B. SSM establishment and analysis 13

50 III.C. Accuracy evaluation and analysis 14

51 [III.D. The influence of network flexibility on segmentation accuracy](#) 18

52 III.E. Comparison with other methods 20

53 **IV. Discussion** **20**

54 **V. Conclusions** **22**

55 **References** **23**

1. Introduction

56

roduction

57 With Magnetic Resonance (MR) imaging becoming an increasingly important non-invasive
58 imaging modality^{b1}, prostate MR segmentation has been paid close attention in recent years,
59 as it is crucial for the clinical diagnosis, therapeutic procedure, and treatment planning
60 of various prostate disorders (e.g., prostate cancer, prostatitis or prostatic hypertrophy)^{b2}.
61 For example, prostate delineation is widely applied for the precise localization of prostate
62 boundary in radiotherapy for dose planning. Besides, in the image-guided computer-assisted
63 surgery, the segmentation of the prostate on preoperative MRI is an essential reference for
64 the inter-operative low-quality image, like ultrasound image^{b3}. However, until now prostate
65 on MR images is still mostly segmented manually by radiologists. The handcrafted delin-
66 eation of prostate boundary is a time-consuming and labor-intensive operation with a low
67 reproducibility because of its high dependence on medical experience. Moreover, those prob-
68 lems are further aggravated when the borderline is indistinct. As pointed out by Yu et
69 al.^{b4}, automatic prostate segmentation is also a challenging task due to the issue of intensity
70 inhomogeneity, variation of anatomical appearance, and lack of boundary discriminability.

71 In order to address this challenging task, different automatic or semi-automatic seg-
72 mentation approaches have been reported in recent years. Martin et al.^{b5, b6} proposed a
73 semi-automatic prostate segmentation method, in which a rigid intensity-based registra-
74 tion algorithm and a non-rigid hybrid registration framework were employed successively to
75 align an atlas to the patient image. In their work, 18 MRI series were involved to construct
76 the atlas. Two accuracy metrics respectively based on volume and surface distance were
77 used to investigate the segmentation performance. Results showed that the segmentation
78 accuracy of the apex region and the central region is higher than the base part. In an-
79 other publication, to add additional knowledge into the segmentation procedure, Korsager
80 et al.^{b7} combined the spatial information of a prostate atlas with the intensity information
81 in a graph cut segmentation framework to achieve automatic prostate delineation. Their
82 validation experiment was investigated on 76 axial MR images. As a result, a mean Dice
83 similarity coefficient (DSC) of 0.88 and a mean surface distance of 1.45 mm were reported.
84 Besides, Tian et al.^{b8} utilized a superpixel-based graph cut framework to acquire the prostate
85 surface on MRI. A superpixel is a group of pixels that have similar characteristics such as
86 intensity or location. Due to the capacity to carry wider information, serving as a more

87 convenient and compact representation of the original image, the superpixel image has been
88 widely used in image segmentation algorithms. In Tian’s study, a graph cuts algorithm and
89 an active contour model were integrated for cross-promotion. According to their experiment
90 results, the verification on 43 MRI examples obtained a mean dice of 0.893.

91 Recently, the performance of deep learning approaches has outperformed to the tradi-
92 tional state-of-the-art methods in many fields, especially in computer vision^{b9, b10} and medical
93 image processing^{b11, b12}. In those researches, neural networks often work as information ex-
94 tractors to eliminate the tedious procedure of traditional feature choice and collection. For
95 precise segmentation of MRI prostate, Guo et al.^{b13} used more concise and effective hierar-
96 chical features from MRI prostate image by utilizing a stacked sparse autoencoder. Based
97 on the extracted features, a sparse patch matching method was employed to deduce the
98 corresponding prostate likelihood map, which was further combined with a sparse shape
99 model for the final segmentation. Besides, Mun et al.^{b14} integrated encoding, bridge, decod-
100 ing, and classification modules to develop a baseline convolutional neural network (CNN)
101 to extract volumetric information. In the meantime, Jia et al.^{b15} researched a coarse-to-fine
102 algorithm for MRI prostate segmentation through a deep learning method. In their algo-
103 rithm, a registration-based segmentation was firstly used to obtain a rough prostate region.
104 Then a pixel-wise recognizer based on a neural network was further adopted to classify the
105 prostate boundary from the image background. Finally, a refinement algorithm was applied
106 to smooth the contour. Similar to Jia’s work, He et al.^{b16} exploited another coarse-to-fine
107 prostate segmentation system via different algorithms. They firstly proposed an adaptive fea-
108 ture learning probability boosting tree for prostate pre-segmentation. Next, a CNN method
109 was developed to obtain the prostate profile model by the judgment of the inner, external,
110 and boundary points. For the last step, an active shape model was employed for the final
111 surface refinement. Their results showed the method is accurate and robust for prostate
112 segmentation, as the neural network was utilized for the extraction of latent image features
113 and the prediction of the prostate boundary. In addition, Wang et al.^{b17} introduced a 3D
114 deep-supervised full CNN with group dilated convolution, aiming to preserve extra image
115 information for prostate delineation. Their method achieved a dice of 0.86. Generally, the
116 aforementioned methods demonstrated that compared with the traditional segmentation al-
117 gorithms, the approaches based on the deep learning method can delineate the target more
118 accurately in less time. However, the aforementioned ways only involved the information of

119 the specific input image while without any prior knowledge constraints that are potentially
120 helpful to improve the prostate segmentation accuracy.

121 Statistical shape model (SSM) is a geometric model containing a mean shape and mul-
122 tiple compressed primarily shape variations of a collection of similar shapes. Due to the
123 ability to represent prior geometric information, SSM has been widely applied in different
124 medical modalities for the segmentation and registration of various anatomical structures,
125 including brain, bone, liver, heart, prostate and so on^{b18b21}. In this paper, based on a
126 registration approach, we proposed a novel segmentation algorithm to tackle the prostate
127 extraction problem by combining a boundary predictor and a label classifier. Specifically,
128 a GoogLeNet-based branch (SSM-Net) was involved as the boundary predictor to deduce
129 the prostate contour to obtain a boundary distance map, serving as the target contour con-
130 straints. Meanwhile, a 3D residual U-net branch (ResU-Net) was employed as the label
131 classifier to predict a probability label map from the input images, to judge the class pos-
132 sibility of each pixel. In the inference step, the optimal weighted sum of the distance map
133 and the probability map was regarded as the final prostate segmentation. In our validation
134 experiment, six different SSMs with various nodes were built to investigate the accuracy and
135 efficiency of the whole algorithm.

136 II. Materials and methods

137 Fig. ^{figure1} [I](#) is an overview of the proposed prostate segmentation algorithm. The segmentation
138 network comprises two branches, serving as a boundary predictor and a label classifier re-
139 spectively. As shown by Fig. ^{figure1} [IA](#), the first SSM-Net branch is used to deduce from the
140 input, three variables: the SSM global transform, shape control parameters, and the point-
141 wise fine-tuning vector. Then, a patient-specific deformation field is calculated based on the
142 predicted variables, and a surface of target is further generated via a coordinate sampler.
143 The second ResU-Net branch is employed to predict a probability label map from the input
144 images, instead of directly using its binarized result as the target region. The parameters of
145 the whole network can be optimized by minimizing the loss function value, which is related
146 to two parts (Sec. ^{sec::section2.4} [II.D](#)): 1) the dice coefficient between the predicted probability map and
147 the input binary label, defined as Loss 1. 2) the similarity between the SSM deformed surface
148 and the input prostate, defined as Loss 2. In the inference phase(Fig. ^{figure1} [IB](#)), according to the

149 generated contour obtained by deforming the SSM by using the deformation field predicted
 150 by the SSM-Net branch, a distance map is directly calculated to serve as the target bound-
 151 ary constraints. Then, the weighted sum of the distance map and the probability map is
 152 regarded as the final prostate segmentation.

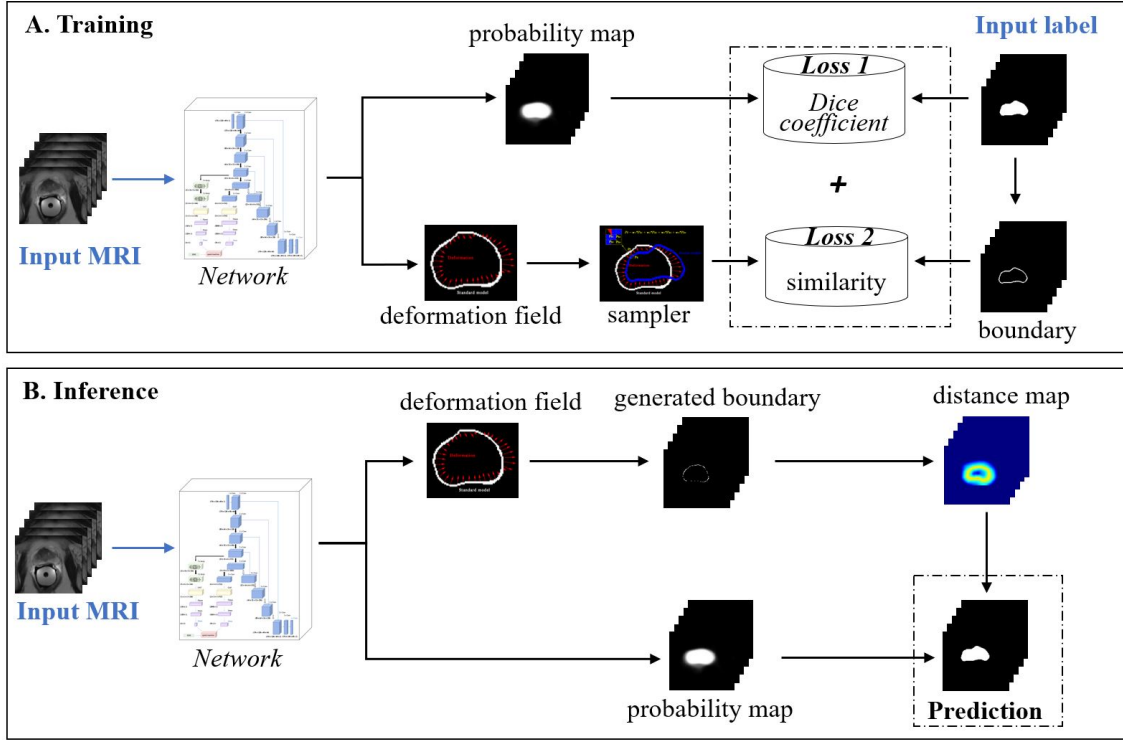


Figure 1: The overview of the proposed prostate segmentation framework.

figure1

153 II.A. Statistical shape model

ection2.1

154 Due to the capacity to carry prior geometric information of numerous examples in differ-
 155 ent medical modalities, SSM has been widely applied in object recognition, image process,
 156 surgery implant design^{b22}. Generally, it involves two parts to describe the statistical spatial
 157 information of a collection of objects: a geometric model for the representation of the mean
 158 shape, and a series of variation vectors to depict the principal components of divergences
 159 between the objects and the mean shape. As the most prevalent SSM type, Principal Com-
 160 ponent Analysis (PCA) based shape model can model the variability of various types of
 161 objects such as images, displacement fields, surface meshes, and volumetric meshes. In our

work, we built PCA SSMs based on triangulated surface meshes, to represent the prostate surface on the patient image. For the prostate, the procedures of building the PCA model can be summarized as following steps: 1) Segment the target from the original image volume. 2) Construct and refine 3D surface triangle mesh based on the binary target label. 3) Subdivide and decimate the meshes to a specific number of points. 4) Transform the meshes to the same posture and align them correspondingly. 5) Establish PCA-based SSMs based on the corresponding objects. 6) Augment the SSM flexibility by employing a Gaussian process.

Table 1 Table 1: Mathematic notations of statistical shape model

A. Variables: scalars, vectors, matrices	
N	Number of SSM nodes
M	Number of SSM variations
$\bar{u}_{3N \times 1}(\bar{u}_{3N})$	SSM mean shape
$\psi_{3N \times M}$	SSM variation / PCA basis
$\kappa_{M \times 1}(\kappa_M)$	Variance of SSM variations
$\theta_{M \times 1}(\theta_M)$	SSM shape control parameters
$t_3 : T, R$	Transform parameters: translation and rotation
$I_{3 \times 3}(I)$	Identity matrix
B. Operators and functions	
$diag(\vec{v})$	Diagonal matrix of vector \vec{v}
$V(\psi_{3N \times M}, \kappa_M, \theta_M, \bar{u}_{3N})$	Model surface deformation

According to the theory of the PCA-based model, an arbitrary shape can be represented by superimposing a deformation field to the mean shape. In our work, a deformation field is described as the sum of global transform, weighted variations, and the mean shape. That means, according to the notations defined in Table [1](#), shape can be written as follows:

$$\begin{aligned} u' &= \bar{u}_{3N} + V(\psi_{3N \times M}, \kappa_M, \theta_M, t_3) \\ &= \bar{u}_{3N} + \psi_{3N \times M} \cdot diag(\kappa_M) \cdot \theta_M \cdot R + T \end{aligned} \tag{1} \quad \text{equation1}$$

The deformation ability of SSM depends on its node number (N) and the variation matrix $\psi_{3N \times M}$. As only very limited datasets were used to build the SSM, the model is insufficient to explain all possible shape variations. Two approaches were employed to solve this problem. Firstly, according to the principle of statistic shape, augmenting the example

178 shapes by involving small and very smoothly varying deformations, can make the variation
 179 matrix (noted as $\psi_{3N \times M} \cdot \text{diag}(\kappa_M)$ in Eq. [\(1\)](#)) more representative. $\psi_{3N \times M} \cdot \text{diag}(\kappa_M)$ is
 180 PCA dimensionality reduction form of variation matrix $\psi_{3N \times M}$.

$$\psi_{3N \times 3N} = \begin{bmatrix} k_{SSM}(x_1, x_1) & \cdots & k_{SSM}(x_1, x_N) \\ \vdots & \ddots & \vdots \\ k_{SSM}(x_N, x_1) & \cdots & k_{SSM}(x_N, x_N) \end{bmatrix} \quad (2) \quad \text{equation2}$$

$$k_{SSM}(x, x') = \frac{1}{n-1} \sum_{i=1}^n (u_i(x) - \mu_{SSM}(x))(u_i(x') - \mu_{SSM}(x'))^T \quad (3) \quad \text{equation3}$$

181 Combining sample covariance kernel ($k_{SSM}(x, x')$) calculated from sample data, and
 182 Gaussian kernel $k_g^{(s, \sigma)}$ can enlarge the flexibility of the model. For the Gaussian kernel in
 183 this paper, the smoothness $\sigma = 10mm$ and the scale of the deformation $s = 2mm$.

$$k_{aug}(x, x') = k_{SSM}(x, x') + k_g^{(2, 10)}(x, x') \quad (4) \quad \text{equation4}$$

$$k_g^{(s, \sigma)}(x, x') = s \cdot \text{diag}(\exp(-\frac{\|x - x'\|^2}{\sigma^2})) \quad (5) \quad \text{equation5}$$

184 Secondly, supplementing a point-by-point item ξ_{3N} to the deformed target (u') was
 185 another feasible approach to represent more possible targets, as shown as Eq. [\(6\)](#). Item ξ_{3N}
 186 was predicted by the SSM-net branch automatically. As shown in Figure 2, the prediction of
 187 the offset vector shared the same residual CNN structure as the prediction of shape control
 188 parameters (noted as θ_M in Eq. [\(6\)](#)).

$$\begin{aligned} u' &= \bar{u}_{3N} + V(\psi_{3N \times M}, \kappa_M, \theta_M, t_3) + \xi_{3N} \\ &= \bar{u}_{3N} + \psi_{3N \times M} \cdot \text{diag}(\kappa_M) \cdot \theta_M \cdot R + T + \xi_{3N} \end{aligned} \quad (6) \quad \text{equation6}$$

189 The surface model is commonly defined in the physical spatial coordinate system to
 190 maintain the visualization invariance on different platforms. The transformation between
 191 model space and image space in this work is shown as follows:

$$P_i = \lfloor (P_m - P_0)/s + 0.5 \rfloor \quad (7) \quad \text{equation7}$$

192 where s is the image resolution, and P_0 is the position of image origin in the physical
 193 spatial coordinate system. P_m indicates the coordinate of model node m in spatial space
 194 and P_i is the corresponding coordinate of P_m in image space.

195 II.B. CNN architecture of the segmentation framework

section2.2

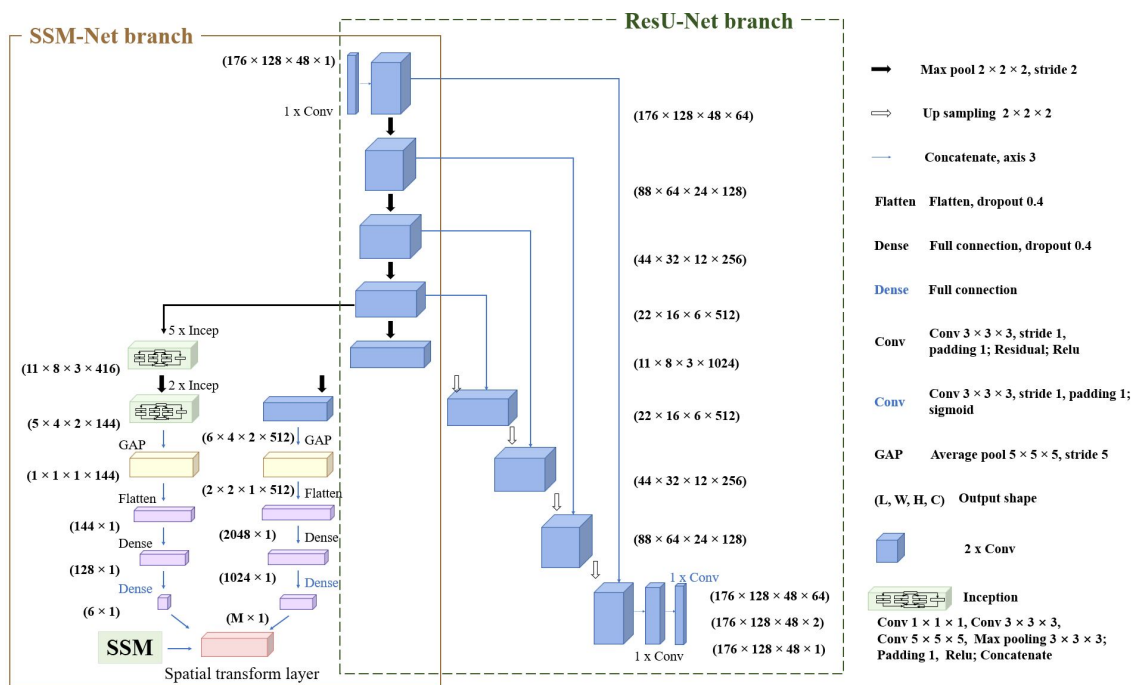


figure2

Figure 2: The structure of the whole network.

196 This subsection describes the architecture of the network involved in our segmentation
 197 framework. As illustrated in Fig. [figure2](#), the input image was size of $(176, 128, 48, 1)$. For
 198 the SSM-Net branch, the inception block of GoogLeNet was utilized for the extraction of
 199 the prostate position. There, GoogLeNet²³ is a CNN originally designed for the ILSVRC
 200 (ImageNet Large Scale Visual Recognition Competition). Its adopted inception blocks are
 201 composed of several convolutional filters of various sizes, making easier the exploration of
 202 image details at different scales. On the basis of the original GoogLeNet, a dense layer with
 203 a size of 128 is connected to its flatten layer, for the prediction of the global transform $(D_x,$
 204 $D_y, D_z, R_x, R_y, R_z)$, including three parameters for translation and three parameters for
 205 rotation, as shown by the left column of SSM-Net branch in Fig. [figure2](#). The right column of
 206 the SSM-Net branch in Fig. [figure2](#)A shows the network structure for the prediction of shape

control parameters with the size of $M \times 1$ (M is the number of shape variations). The involved convolution layers following the "contracting path" with the kernel size $3 \times 3 \times 3$ used 1 pixel stride, and the employed max-pooling layers used pooling size of 2. Similarly, the prediction of fine-tuning vector shared the same residual CNN structure, expect that the average pooling layer is replaced by a max-pooling layer with the pooling size of 2, the stride of 2. In the last step of the SSM-net branch, the variables including the transform matrix, the shape control parameters, and the fine-tuning vector, are input to the last spatial transformation layer, to yield the prostate contour.

As illustrated by the ResU-net branch in Fig. [figure2](#), a residual U-Net is employed to infer the probability label map. U-net^{b24} is a widely used network with high accuracy for object segmentation. In our segmentation framework, each residual block consists of two convolution layers with a kernel size of $3 \times 3 \times 3$, pixel stride of 1. And the max-pooling layers use a pooling size equal to the stride and the size of the up-sample layers is set to 2. The sigmoid function is utilized as the activation function of the last layer to limit output values to $[0,1]$. For the whole network, the structure of each layer is shown in Fig. [figure2](#).

II.C. Grid mapping

As shown in the overview of the segmentation framework (Fig. [figure1](#)), the patient-specific prostate shape can be obtained by superimposing the predicted deformation field to the standard SSM surface in the inference procedure. While in the training phase, in order to calculate the loss, a predicted binary surface image for SSM (annotated as "generated model surface" in Fig. [figure1](#)) is generated by interpolating the input boundary based on the deformation field.

The output binary surface of SSM $g^t \in \mathbb{R}^{L^t W^t H^t}$ is defined on a regular grid $G^t = \{G_i^t\} = \{(x_i^t, y_i^t, z_i^t)\}, i \in [L^t W^t H^t]$, where L^t, W^t, H^t represent the length, width and height of the output. Similarly, let $G^s = \{(x_i^s, y_i^s, z_i^s)\}, x_i^s \in [0, L^s], y_i^s \in [0, W^s], z_i^s \in [0, H^s]$ be the input grid, where, L^s, W^s, H^s are the length, width and height of the input binary mask respectively. The relationship between the output grid G^t and the input grid G^s can be written as follows.

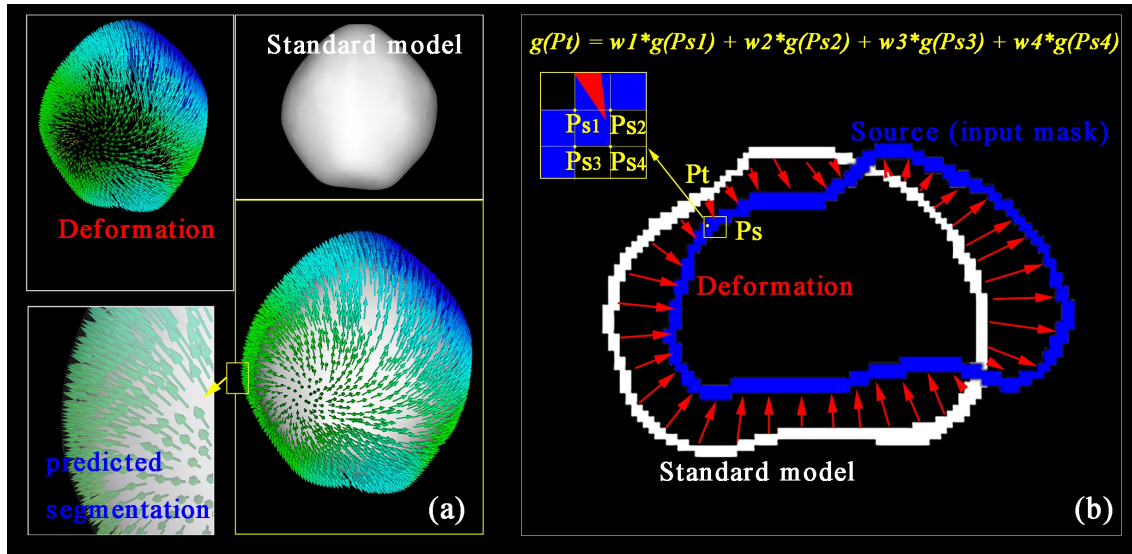


Figure 3: The schematic diagram of segmentation generation and image interpolation. (a) shows that the spatial structure of a predicted segmentation is equal to the sum of the SSM and a deformation field. (b) illustrates the 2D calculation strategy of the gray value on the model boundary according to the binary input mask and the deformation field. indicated with red arrows. $g(P)$ represents the gray value of point P.

figure3

For $\forall i \in [1 \dots L^t W^t H^t]$,

$$G_i^s = D_i(G_i^t) = \begin{pmatrix} x_i^t + d_{i,x} \\ y_i^t + d_{i,y} \\ z_i^t + d_{i,z} \end{pmatrix} = \begin{pmatrix} x_i^s \\ y_i^s \\ z_i^s \end{pmatrix} \quad (8) \quad \text{equation8}$$

229 $D_i(G_i^t)$ is the deformation field predicted by SSM-Net branch, with size of $L^t \times W^t \times$
 230 $H^t \times 3$. Based on Eq. (8), for each node in the output grid, we can trace its corresponding
 231 position on the input mask according to the deformation field. It means that the gray
 232 value of output point $G_i^t = (x_i^t, y_i^t, z_i^t)$ depends on the gray value of the relevant position
 233 $G_i^s = (x_i^s + d_{i,x}, y_i^s + d_{i,y}, z_i^s + d_{i,z})$ in the input mask.

section2.4

II.D. Loss function

235 The loss function of the proposed network consists of two parts: the part for SSM-Net branch
 236 and the part for ResU-Net branch.

For SSM-Net branch, according to the mean shape of SSM and the predicted deforma-

tion field, we can calculate the final segmentation directly. To evaluate the accuracy of the prediction, the specific energy function of SSM-Net branch was employed to optimize the deformation field, which is described as follows:

$$\begin{aligned} E &= L(g^t \diamond G^s) + \lambda \|\varphi\| \\ &= L(g^t \diamond G^s) + \lambda_1 \|\theta\| + \lambda_2 \|t\| + \lambda_3 \|\nabla \xi\| \end{aligned} \quad (9) \quad \text{equation9}$$

237 where g represents the gray label in image space. Specifically, g^t denotes the boundary of
238 the input mask, and (θ, t, ξ) is the predicted deformation field. In this paper, we defined L
239 as:

$$L(g^t \diamond G^s) = 1 - (g^t \diamond G^s)/N \quad (10) \quad \text{equation10}$$

Then, the optimization function can be written as follows:

$$\varphi = (\theta, t, \xi) = \arg \min(1 - (g^s \diamond G^t)/N) + \lambda_1 \|\theta\| + \lambda_2 \|t\| + \lambda_3 \|\nabla \xi\| \quad (11) \quad \text{equation11}$$

240 where N represents the node number of SSM.

To obtain $g^t \diamond G^s$, an interpolation is required to calculate the gray value of arbitrary position $G_i^s = (x_i^s, y_i^s, z_i^s)$. In this work, 3D bilinear interpolation method^{b25, b26} is employed. Let g_i^t represents its gray level at point $G_i^t = (x_i^t, y_i^t, z_i^t)$. $g_i^t \diamond G_i^s$ mean the gray level at point $G_i^s = (x_i^s, y_i^s, z_i^s)$, and $\{(m, n, p)\}^s$ represents the point (m, n, p) of input mask respectively. According to Eq. (4), For $\forall i \in [1 \dots L^t W^t H^t]$,

$$\begin{aligned} g_i^t \diamond G_i^s &= g_{(x_i^s, y_i^s, z_i^s)}^s = \sum_m^{L^s} \sum_n^{W^s} \sum_p^{H^s} g_{(m, n, p)}^t \cdot \max(0, 1 - |x_i^s \\ &\quad - m|) \cdot \max(0, 1 - |y_i^s - n|) \cdot \max(0, 1 - |z_i^s - p|) \end{aligned} \quad (12) \quad \text{equation12}$$

The partial derivatives with respect to gray $g_{(m, n, p)}^t$ and coordinate position (x_i^t, y_i^t, z_i^t) for the backpropagation of loss can be written as follows ($\partial g_i^t \diamond G_i^s / \partial y_i^s$, $\partial g_i^t \diamond G_i^s / \partial z_i^s$ are similar with $\partial g_i^t \diamond G_i^s / \partial x_i^s$):

$$\begin{aligned} \frac{\partial g_i^t \diamond G_i^s}{\partial g_{(m, n, p)}^t} &= \sum_m^{L^s} \sum_n^{W^s} \sum_p^{H^s} \max(0, 1 - |x_i^s - m|) \cdot \\ &\quad \max(0, 1 - |y_i^s - n|) \cdot \max(0, 1 - |z_i^s - p|) \end{aligned} \quad (13) \quad \text{equation13}$$

$$\frac{\partial g_i^t \diamond G_i^s}{\partial x_i^s} = \sum_m^{L^s} \sum_n^{W^s} \sum_p^{H^s} g_{(m,n,p)}^t \cdot \max(0, 1 - |y_i^s - m|) \cdot \max(0, 1 - |z_i^s - p|) \cdot \begin{cases} 0, & |x_i^s - n| > 1, \\ -1, & x_i^s > n, \\ 1, & x_i^s < n. \end{cases} \quad (14) \quad \text{equation14}$$

For ResU-Net branch, the following loss function is adopted, where, S_{mask} represent the ground truth. ϑ is the network parameters and P_{ResU} is the output probability map. The values of range from 0 to 1.

$$L(\vartheta, S_{mask}) = 1 - \frac{2 \times \|P_{ResU}(\vartheta) \times S_{mask}\|}{\|P_{ResU}\| + \|S_{mask}\|} \quad (15) \quad \text{equation15}$$

Thus, the parameterized ResU-Net branch can be optimized during the training procedure:

$$\hat{\vartheta} = \arg \min_{\vartheta} L(\vartheta, S_{mask}) \quad (16) \quad \text{equation16}$$

241 Based on Eq. [\(10\)](#) and Eq. [\(15\)](#), the loss function of the whole network is defined as
 242 Eq. [\(17\)](#), to optimize the network weights. Where α and β are trainable parameters.

$$L_{combined} = \alpha L(l, M, \phi) + \beta L(\vartheta, S_{mask}) \quad (17) \quad \text{equation17}$$

243 section2.5 II.E. Inference of prostate region

In the prostate inference step, the binarized weighted sum of the deduced probability map and distance map is regarded as the final prostate segmentation. In terms of probability label map, a bigger value means a higher probability for a pixel to belong to the prostate region. The distance map obtained from the boundary image predicted by the SSM-branch, is such that only the pixel on the boundary has a value of 1, while others are equal to 0. It is calculated according to the following equation:

$$D_{ssm}(P_i) = 1 - \|P_i - \hat{P}_i\|/10 \quad (18) \quad \text{equation18}$$

244 where, P_i represents pixel i , $D_{ssm}(P_i)$ is the value of P_i on the distance map. \hat{P}_i is the
 245 closest boundary point of P_i on the input boundary image, and $\|P_i - \hat{P}_i\|$ is the Euclidean

246 distance between P_i and \hat{P}_i . 10 is the calculation range, which should be changed according
 247 to the image resolution because it decides the prostate voxel range in images. As the image
 248 volume was resampled to the same resolution, the calculation range is a constant in our
 249 work. Furtherly, as the interior prostate gland being segmented should be evaluated with a
 250 large value to reflect its high probability, for the pixel P_i in the interior region with $D_{ssm}(P_i)$
 251 less than 0.5, its D_{ssm} value is reassigned to 1.

The probability map generated by the Res-UNet branch is such that the central region of the prostate has a probability of 1 whilst the marginal prostate region is valued with a lower value, which contributes to most of the prediction deviation, especially when the contour of the prostate is indistinct. In contrast, in this case, the SSM-Net branch can deduce a relatively reasonable boundary due to the representation of prostate shape prior and provided complementary information for the result of the ResU-Net branch. However, the distance map calculated from the SSM-Net branch might not match the segmentation results from the ResU-Net branch, therefore, we have investigated the segmentation performance of the proposed method under different combinations of SSM-Net and ResU-Net branches, as shown as follows:

$$P_{combined} = w_1 P_{ResU} + (1 - w_1) D_{ssm} \quad (19) \quad \text{equation19}$$

Two metrics were introduced to evaluate the performance of the proposed segmentation framework, including the dice similarity coefficient (DSC) and the average over the shortest distance between the boundary points of the volumes(ABD). The DSC is formulated as follows:

$$Dice = 2 * \|S_{pred} \cap S_{mask}\| / (\|S_{pred}\| + \|S_{mask}\|) \quad (20) \quad \text{equation20}$$

252 where S_{pred} and S_{mask} respectively present the predicted segmentation and the input ground
 253 truth.

254 III. Results

255 III.A. Data acquisition and experiment set up

256 We validated the proposed network on two public datasets: the MICCAI PROMISE12 chal-
 257 lenge dataset^{b27} and NCI-ISBI 2013 challenge dataset^{b28}. The first database contains 50

258 prostate transversal T2 MRIs for training and 30 prostate images for testing. And the second
 259 database respectively involves 60, 10, and 10 cases for training, leaderboard, and testing.
 260 The two datasets share 11 common volumes, and the ground truths of the PROMISE12
 261 testing set are unavailable. Thus, a total of 119 T2 MRI image cases are collected for our
 262 experiment. As the gathered data have different voxel spacing and image size, the input
 263 images were resized to the shape of $176 \times 128 \times 48$ beforehand.

264 From the 119 volumes, 40 randomly selected cases contributed to the SSM establish-
 265 ment, and the rest data were used for the network optimization. Specifically, 63 out of
 266 the 79 image volumes (3/4) were applied for the network training and the remaining (1/4)
 267 for the validation. The modeling procedure and the network segmentation performance are
 268 illustrated in Section [III.B](#) and Section [III.C](#) respectively. And Section [III.D](#) analyzes and
 269 discusses the influence of SSM flexibility on the framework segmentation accuracy. The net-
 270 work training and all experiments were conducted on a computer with Intel® Core (TM)
 271 I7-8700K with a 3.70 GHz CPU, 8 GB memory, and two graphic cards of 8GB NVIDIA
 272 GeForce GTX 1080 Ti.

273 III.B. SSM establishment and analysis

section3.2

274 The node number and the principal component number are two dominant factors for the flex-
 275 ibility of SSM. The former is decided according to the node number of the counted meshes,
 276 and the latter is determined by the compactness of SSM. The compactness is measured via
 277 the accumulation of SSM variations which are arranged according to their eigenvalues. In
 278 this work, we selected the first M principle components to keep 95% of the total eigenvalues.
 279 To investigate the influence of the two factors on the segmentation accuracy of the seg-
 280 mentation method, six SSMs with various nodes and principal components were built. 3D
 281 slicer (<https://www.slicer.org>) was utilized for the refinement of 3D surfaces. In addition,
 282 the Gaussian process model building, model fitting, and the PCA-based model building are
 283 completed via the Statismo library [\[22\]](#). The details of SSMs are presented in Table [2](#). The
 284 third column shows the models after flexibility augmentation.

Table 2: The details of statistical shape models with various number of nodes

Number of nodes	Original SSMs	Augmented SSMs
	Variation(3N x M)	Variation(3N x M)
1625	4875 × 49	4875 × 50
3250	9750 × 49	9750 × 50
6500	19500 × 49	19500 × 50
9750	29250 × 49	29250 × 50
13000	39000 × 48	39000 × 50
16250	48750 × 47	48750 × 50

III.C. Accuracy evaluation and analysis

ection3.3

Figure 4 illustrates the flexibilities of the primary SSMs. The green models in the middle column depicts the mean shapes with increasing node numbers from top to bottom. From the middle to the rightmost, the three columns respectively exhibit the deformed shapes generated from the mean shape of SSM by weighting the first three principal variations with three times of their corresponding deviations. Accordingly, the three-column shapes on the left describe the generated models deformed by negative triple deviations. Generally, each row horizontally reveals the influence of the first three principal variations on the deformation of each SSM, and each column vertically compares the different performances of SSMs. In conclusion, the last three SSMs with node numbers of 9750, 13000, 15250 had similar interior and exterior characteristics, while the first three SSMs behaved quite differently.

Based on Eq. (17), the network weights was optimized via Adam optimizer with the learning rate ranged from 10^{-5} to 1, and the three regularization coefficients λ_1 , λ_2 and λ_3 ranged from 0 to 1 respectively. During the training period, we compared the performance of the proposed segmentation framework applying different values of regularization coefficients λ_1 , λ_2 and λ_3 in Eq. (11). The experiments showed that the best result in terms of the Dice coefficient is achieved when λ_1 , λ_2 , and λ_3 are equal to 0, 0.01, and 0.01. In the following work, λ_1 , λ_2 and λ_3 are set to 0, 0.01, and 0.01. In addition, we figured out the proposed segmentation framework performs best when the “hyperparameter” w_1 in Eq. (19) equals 0.6 by trial and error.

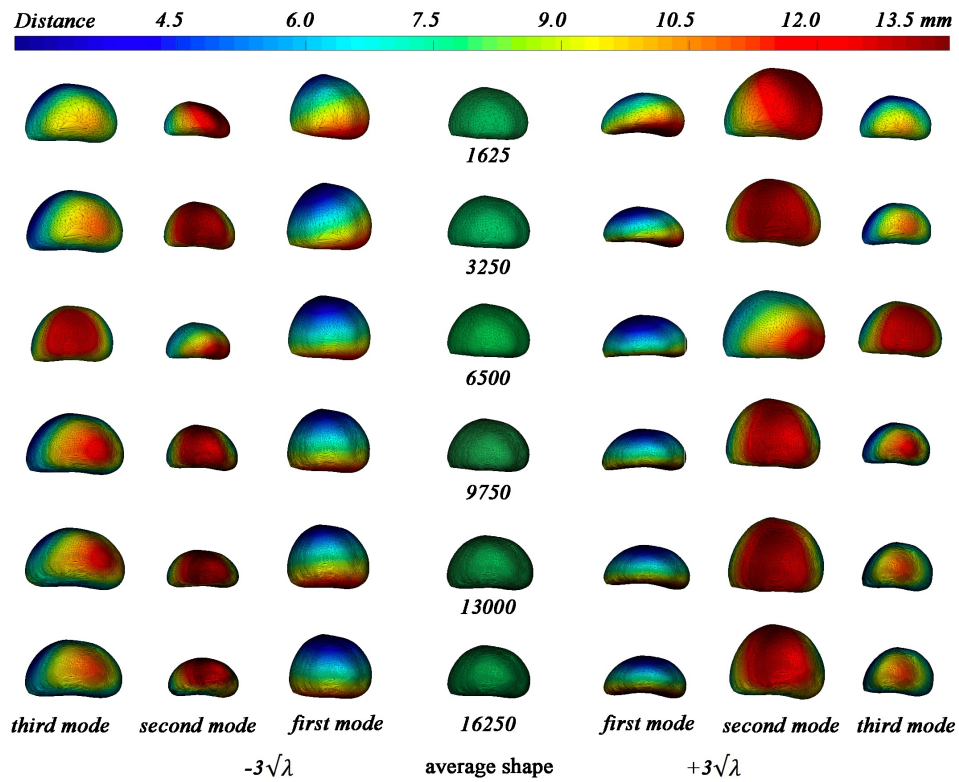


Figure 4: The flexibility of the statistical shape models with different node numbers. The middle column with green color exhibits the mean models, and the left three columns and the right three columns respectively show the deformed models drove by $3\sqrt{\lambda}$ times of the first three principal components of variations. λ is the corresponding deviation of each component.

figure4

306 Fig. [figure5](#) illustrates the DSC and ABD of the proposed prostate segmentation framework
 307 when adopted different SSMs. 4-fold cross-validation was conducted for each group. The
 308 DSC and ABD of the ResU-Net branch are constant over the different groups. In terms
 309 of the SSM-Net branch, when the network adopts SSMs with 1625 to 9750 nodes (referred
 310 as network nodes in the following text), the dice result has significant improved from 0.69
 311 to 0.90 (paired t-test, $p < 0.001$). At the same time, the ABD value has an opposite steep
 312 trend, decreasing from 2.63 mm to 2.39 mm. Both dice and ABD have the best result when
 313 network node number is 9750, with an average dice of 0.862 and an ABD of 2.04 mm. As
 314 regards the performance of the whole framework, it has a similar trend with the SSM-Net
 315 branch, with the dice reached a peak of 0.907 and the ABD declined to the lowest of 1.85
 316 mm. For the two groups with more than 9750 nodes, they performed slightly inferior with a

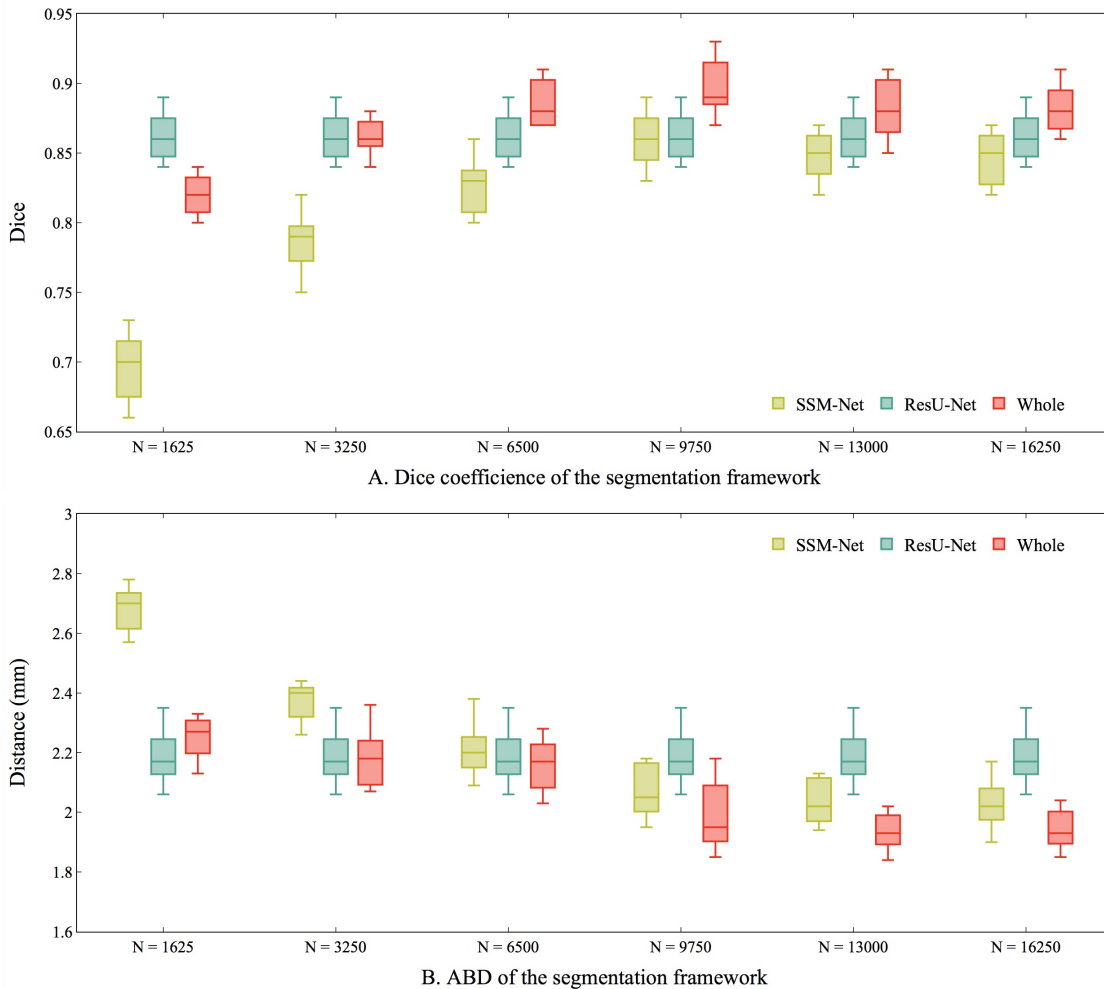


Figure 5: The DSC and ABD results of the whole framework, SSM-Net branch, and ResU-Net branch respectively.

figure5

317 dice of 0.89. According to the record data, we concluded that the SSM with 9750 nodes is
 318 optimal to employ in our framework for the representation of the prostate spatial boundary.

319 The segmentation procedure of the proposed framework is shown in Fig. [figure6](#)
 320 model in (c) represents the SSM, whose center is initially positioned at the origin (0,0,0) of the
 321 anatomical coordinate system of LPS (Left, Posterior, Superior). As shown in (c), according
 322 to the input image, the SSM-Net branch respectively predicts the global transform, weight
 323 parameters, and an offset vector for the calculation of the deformation field. The 3D white
 324 surface in (d) represents the generated prostate boundary by applying the deformation field
 325 to the SSM. Fig. [figure7](#) illustrates the delineation results of four images series. Four slices range
 326 from number 16 to number 46 with an interval of 10, are selected to display the recognition

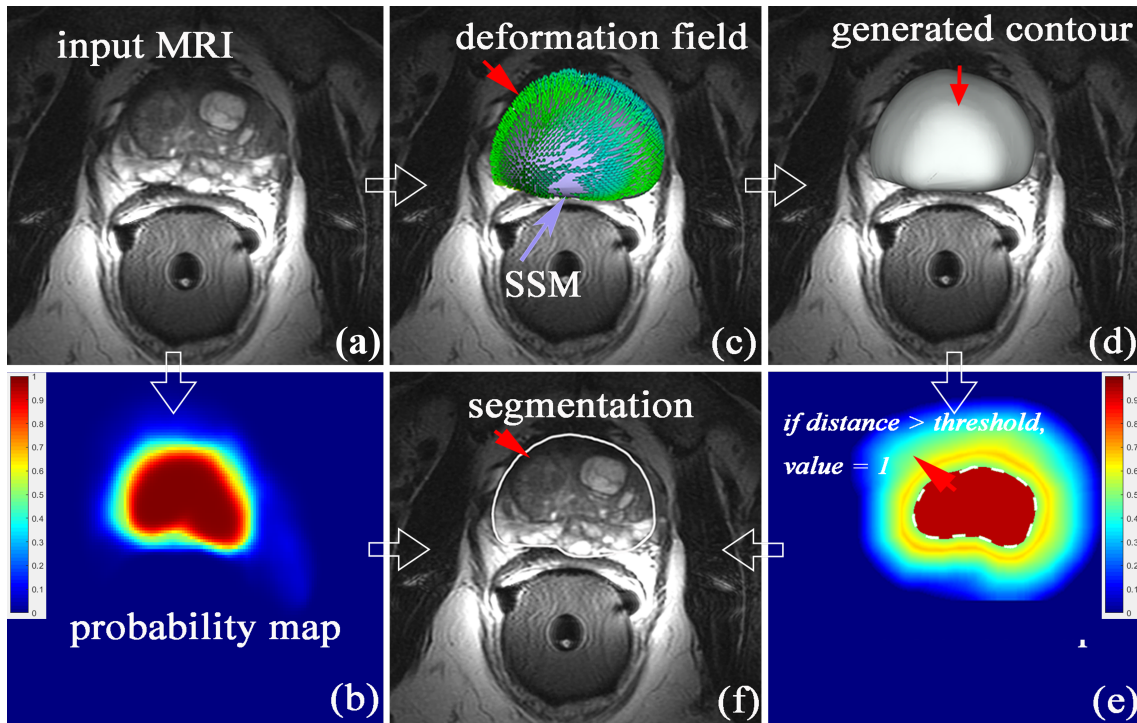


Figure 6: The whole segmentation procedure. (a) The input MR image for segmentation. (b) The probability map. (c) The purple model represents the SSM, whose center initially positioned at the origin (0,0,0). (d) The generated contour of the prostate from the SSM. (e) The distance map. (f) The segmentation result.

figure6

327 performances on different prostate zones. Each row stands one example, and accordingly,
 328 each column shows the delineation results of the same layers of different examples. From
 329 the exhibition, we deduced that the segmentation on the prostate central zone has higher
 330 accuracy than the base of the prostate (more complex to delineate). For the case of the severe
 331 hyperplastic prostate gland which is larger than the mean shape of SSM, the segmentation
 332 framework has relatively poor performance with the maximum ABD was 2.7 mm and the
 333 dice coefficient was 0.83. Compared to the segmentation approach employing only the SSM
 334 method, our framework can achieve more accurate delineation when the target is beyond
 335 the SSM deformation range.

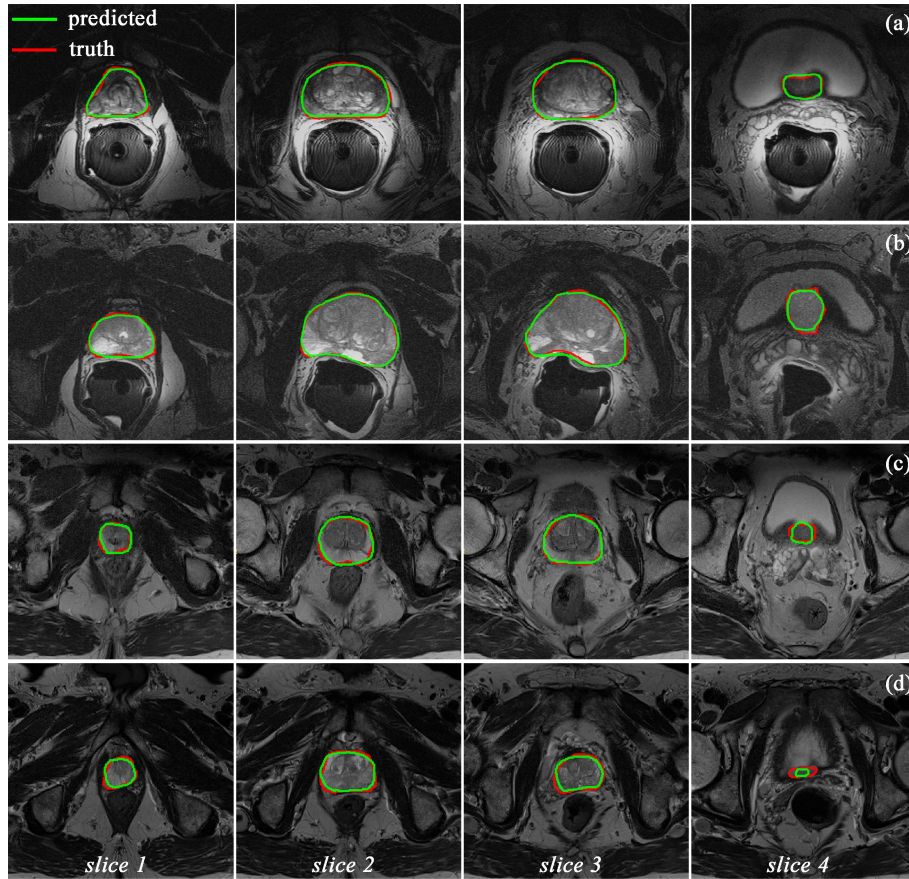


Figure 7: The segmentation results of four image cases via the proposed method. Each row stands one example, and each column shows their segmentation results of the same layers of different examples.

figure7

III.D. The influence of network flexibility on segmentation accuracy

According to the analysis in Section [II.B.](#), [network node number](#), flexibility augmentation of SSM, and fine-tuning item (offset) are the three dominant factors to affect the network deformation ability. To investigate their impacts on the network delineation accuracy, we verified the individual segmentation performance of the SSM-Net branch under different combinations of the three elastic determinants. Fig. [8](#) presents the DSC and ABD values of the SSM-Net branch with various nodes and different utilization situations of augmentation and offset item. As shown by those statistical trend lines, regardless of the model augmentation or fine-tuning item, the SSM-Net branch with 9750 nodes or more outperformed other situations. In terms of the model flexibility augmentation, its application has improved the

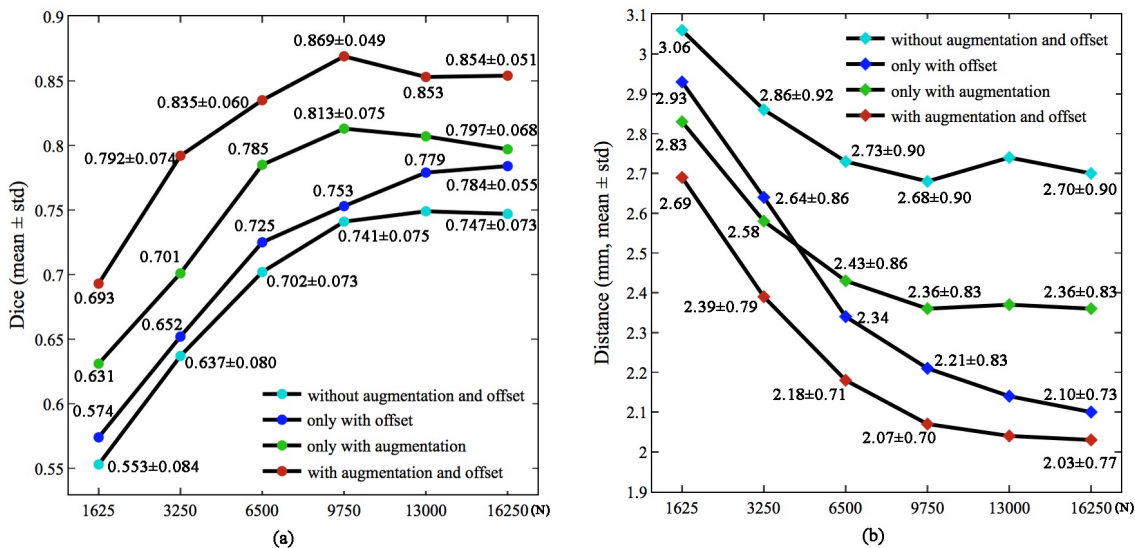


Figure 8: The influence of the deformation ability of SSM-Net branch on its segmentation performances, including dice scores and ABD values). The network elastic ability is mainly determined by three factors: node numbers, flexibility augmentation and the offset item.

figure8

347 network accuracy. As shown by the lines with cyan and blue dots in Fig. [figure8](#), compared
 348 with the results of the network without augmentation and offset, the best average dice and
 349 distance of the network adopting model elastic augmentation were improved to 0.81 and
 350 2.36 mm respectively. And the network employing both augmentation and offset had higher
 351 average dice and smaller average distance than the network utilizing only offset item, as
 352 informed by the lines with green and red dots in the figure. Similarly, we figure out that
 353 the employment of offset item also contributed to the improvement of the SSM-Net branch.
 354 Specifically, compared with the segmentation result of the network without augmentation
 355 (the line with cyan dots in subgraph (a)), the involvement of fine-tuning item (the line with
 356 blue dots in subgraph (a)) increased the highest average dice of the six groups from 0.74
 357 to 0.79. Based on the network which applies only flexibility augmentation (the lines with
 358 blue dots), the utilization of offset items (the lines with red dots) improved the average dice
 359 coefficient by 0.06 and the distance by 0.25 mm, making the SSM-Net branch achieve the
 360 best result.

Table 3: Comparison between our method and other automatic segmentation methods. All the methods were trained and tested on the same dataset.

Table3

Work	Method	DSC + std	ABD [mm])	Time
Maan et al. ^{b32}	3D AAM	0.81 ± 0.13	3.09 ± 0.96	4 min
Vincent et al. ^{b33}	AAM	0.86 ± 0.07	2.17 ± 0.63	8 min
Toth et al. ^{b36}	Deformation landmark AAM	0.77 ± 0.18	3.64 ± 1.39	3 min
Ou et al. ^{b30}	Multi-atlas	0.84 ± 0.06	2.85 ± 0.72	40 min
Gao et al. ^{b31}	Multi-atlas + patch-based voxel	0.82 ± 0.02	2.86 ± 0.82	30 min
Milletari et al. ^{b35}	V-Net	0.86 ± 0.11	2.13 ± 0.86	<1 min
Yu et al. ^{b4}	Volumetric ConvNet	0.87 ± 0.24	2.05 ± 0.69	<1 min
Karimi et al. ^{b34}	CNN + SSM	0.88 ± 0.09	2.16 ± 0.77	<1 min
Tian et al. ^{b37}	PSNet	0.86 ± 0.40	2.72 ± 0.90	<1 min
Jia et al. ^{b38}	Multi-atlas + VGG-19	0.92 ± 0.05	1.63 ± 0.38	40 min
Ours	SSM-Net + ResU-Net	0.90 ± 0.08	1.85 ± 0.75	<1min

III.E. Comparison with other methods

361

section3.5

362 We compared the performance of our method with existing automatic segmentation methods
 363 (including atlas-based method, deformable model-based method, and deep learning-based
 364 method). Non-open-source methods were excluded for comparison. All deep-learning-based
 365 methods are trained on the same dataset (consisting of 63 volumes), and tested on the
 366 same dataset (consisting of 16 volumes). For methods that are not based on deep learning,
 367 their performances are evaluated on the same test dataset (consisting of 16 volumes).. The
 368 comparison results are summarized in Table ^{Table3}3. Results illustrated that our method can
 369 achieve the second best accuracy than other methods. The inference time consumption of
 370 our method is much less than atlas or deformable model based methods, and is comparable
 371 with deep learning network methods.

IV. Discussion

372

:section4

373 Prostate segmentation facilitates the diagnosis and treatment of prostate diseases. For ex-
 374 ample, the determination and location of the prostate region are essential information for
 375 radiotherapy or high-intensity focused ultrasound operations. However, its clinical appli-
 376 cation is still limited, because of the segmentation challenges like inhomogeneous intensity,

377 various anatomical appearances, and indiscernible boundaries. Therefore, in this work, we
378 proposed a novel prostate segmentation framework, based on CNN and SSM, which has been
379 widely used in prostate segmentation^{b29}. The results demonstrate that the network has the
380 optimal dice of 0.907 and DSC of 1.85 mm under the network nodes of 9750. And both model
381 elastic augmentation and offset applications have positive effects. The performance on the
382 collected clinical data demonstrates that our prostate segmentation framework is feasible,
383 and it has the potential to be a useful clinical tool for the diagnosis, treatment design, and
384 therapeutic procedure of variable prostate disease.

385 As shown in Figure 4, driven by their first three principal components of variations,
386 the first four statistical shape models with nodes number from 1625 to 9750 perform quite
387 different from each other, while the two statistic shape models with nodes number of 13000
388 and 15250 have almost similar performance with the model with 9750. Thus, the mesh
389 shape with nodes number of 9750 is accurate enough to represent the anatomical structure
390 of a regular prostate in the physical coordinate system. However, when nodes number is
391 more than 9750, the accuracy (including DSC and ABD) does not improve with the increase
392 of nodes number. That's because when the model owns a substantial number of nodes,
393 one pixel in the image space may correspond to more than one node in the physical space,
394 resulting in decreased performance.

395 In the past three decades, three major categories of automatic prostate segmentation
396 have been introduced, including atlas-based algorithms, deformable model-based approaches,
397 and deep learning-based methods. For the first category, the atlas-based strategy has been
398 widely utilized in medical image segmentation and registration^{b30b31}. Its major principle is
399 to align an atlas that contained spatial prior knowledge to the target images by registration
400 approaches. Then apply the alignment information to deform the atlas label for the final
401 target segmentation. Secondly, in terms of the model-based method, a deformable model is
402 firstly constructed for the representation of standard prostate contour. Then the information
403 extracted from the target image was further applied to drive the model to generate the
404 specific shape. Several groups in the list^{b32b34} employed deformable model (AAM, ASM,
405 SSM) for the prediction of prostate. For the third group, deep learning-based approaches,
406 especially CNNs are widely introduced in medical image processing because of the powerful
407 feature extraction and non-linear learning capability^{b34, b4, b35}.

408 Several teams have combined deep learning algorithms with atlas or deformable models
409 in their researches. Similarly, our segmentation combined neural network with SSM for
410 high precise MRI prostate segmentation. In this way, prior knowledge is introduced by
411 SSM to serve as the boundary constraint and a rough reference, and furtherly combined
412 with a neural network (ResU-Net in our work) which can obtain details from the target
413 image, for the precise recognition of the target region. Besides, as SSM is built based on
414 lots of medical image data, the generated model can reasonably represent the deformation.
415 Therefore, our method required less time (approximately 3 s) while performed a satisfactory
416 segmentation accuracy with high robustness.

417 In medical image processing, the collection of the training dataset limits the application
418 of various learning-based approaches. Fortunately, SSM utilizes geometric information rather
419 than intensity information. Therefore, all images in different modalities such as computed
420 tomography, ultrasound and MRI can contribute to the construction of SSM. It is worth
421 mentioning that, if the dataset is sufficient, active shape model(ASM) and statistical defor-
422 mation models (SDM) could become superior training supervisors than SSM, as the former
423 can carry intensity information of images and the latter is capable to represent the statistical
424 information of deformation field of a collection of examples. In addition, the introduction of
425 the finite element model (FEM) is worth considering for our further development, because
426 the biomechanical information in FEM can contribute to the delineation of a specific target.

427 The proposed method has a very good potential for clinical application. After estab-
428 lishing the SSM model and training the network, the MR images containing the prostate can
429 be segmented automatically. The 3D model of the prostate can be reconstructed from the
430 segmented results, which is useful for morphological analysis, volume calculation, etc. More-
431 over, such workflow can be integrated into our previously developed image-guided surgical
432 system ^{b39, b40} to improve its efficiency and automation.

433 V. Conclusions

:section5

434 In this study, we introduced a novel registration-based algorithm that combines CNN and
435 SSM and applied it to the task of precise prostate segmentation. A two branches structure
436 was designed, through which the prior knowledge introduced by SSM and boundary features

437 extracted by the CNN were fully used for prostate segmentation. Extensive experimental re-
438 sults conducted on two public datasets demonstrated that the proposed network can achieve
439 better performance than several state-of-the-art algorithms for prostate segmentation.

440 Acknowledgments

441 This work was supported by grants from the National Natural Science Foundation of China
442 (81971709; M-0019; 82011530141), PHC CAI YUANPEI Program(41366SA), Agence Na-
443 tionale de la Recherche (Investissements d’Avenir Program – grants ANR-11-LABX-0004 and
444 ANR-19-P3IA-0003), Région Auvergne Rhône-Alpes (ProNavIA project), the Foundation of
445 Science and Technology Commission of Shanghai Municipality (19510712200; 20490740700),
446 Shanghai Jiao Tong University Foundation on Medical and Technological Joint Science Re-
447 search (YG2019ZDA06; YG2021ZD21; YG2021QN72; YG2022QN056), and Hospital Funded
448 Clinical Research(21XJMR02), Xinhua Hospital Affiliated to Shanghai Jiao Tong University,
449 School of Medicine.

450 Conflict of Interest

451 The authors have no relevant conflicts of interest to disclose.

453 References

- 454 ¹ Fütterer JJ, Briganti A, De Visschere P, et al. Can Clinically Significant Prostate Cancer
455 Be Detected with Multiparametric Magnetic Resonance Imaging? A Systematic Review
456 of the Literature. *European Urology*. 2015;68(6):1045-1053.
- 457 ² Litjens G, Debats O, Barentsz J, Karssemeijer N, Huisman H. Computer-Aided Detec-
458 tion of Prostate Cancer inMRI. *IEEE Transactions on Medical Imaging*. 2014;33(5):1083-
459 1092.
- 460 ³ Khallaghi S, Sanchez CA, Rasouljan A, et al. Statistical Biomechanical Surface Regis-
461 tration: Application to MR-TRUS Fusion for Prostate Interventions. *IEEE Transactions*
462 *on Medical Imaging*. 2015;34(12):2535-2549.

- b43** 4 Yu L, Yang X, Chen H, Qin J, Heng P-A, Aaai. Volumetric ConvNets with Mixed Residual Connections for Automated Prostate Segmentation from 3D MR Images. Paper presented at: 31st AAAI Conference on Artificial Intelligence; 2017 Feb 04-09, 2017; San Francisco, CA.
- b57** 5 Martin S, Daanen V, Troccaz J. Atlas-based prostate segmentation using an hybrid registration. *International Journal of Computer Assisted Radiology and Surgery*. 2008;3(6):485-492.
- b60** 6 Martin S, Troccaz J, Daanen V. Automated segmentation of the prostate in 3D MR images using a probabilistic atlas and a spatially constrained deformable model. *Medical Physics*. 2010;37(4):1579-1590.
- b73** 7 Korsager AS, Fortunati V, van der Lijn F, et al. The use of atlas registration and graph cuts for prostate segmentation in magnetic resonance images. *Medical Physics*. 2015;42(4):1614-1624.
- b86** 8 Tian Z, Liu L, Zhang Z, Fei B. Superpixel-Based Segmentation for 3D Prostate MR Images. *IEEE Transactions on Medical Imaging*. 2016;35(3):791-801.
- b98** 9 Goodfellow I, Pouget-Abadie J, Mirza M, et al. Generative Adversarial Networks. *Communications of the Acm*. 2020;63(11):139-144.
- b100** 10 Ren S, He K, Girshick R, Sun J. Faster R-CNN: Towards Real-Time Object Detection with Region Proposal Networks. *IEEE transactions on pattern analysis and machine intelligence*. 2017;39(6):1137-1149.
- b143** 11 Pereira S, Pinto A, Alves V, Silva CA. Brain Tumor Segmentation Using Convolutional Neural Networks in MRI Images. *IEEE Transactions on Medical Imaging*. 2016;35(5):1240-1251.
- b126** 12 Tajbakhsh N, Shin JY, Gurudu SR, et al. Convolutional Neural Networks for Medical Image Analysis: Full Training or Fine Tuning? *IEEE Transactions on Medical Imaging*. 2016;35(5):1299-1312.
- b139** 13 Guo Y, Gao Y, Shen D. Deformable MR Prostate Segmentation via Deep Feature Learning and Sparse Patch Matching. *IEEE Transactions on Medical Imaging*. 2016;35(4):1077-1089.
-

- b142** 14 Mun J, Jang W-D, Sung DJ, Kim C-S, Ieee. Comparison of objective functions in cnn-
493 based prostate magnetic resonance image segmentation. Paper presented at: 24th IEEE
494 International Conference on Image Processing (ICIP); 2017 Sep 17-20, 2017; Beijing,
495 PEOPLES R CHINA.
- b156** 15 Jia H, Xia Y, Cai W, Fulham M, Feng DD, Ieee. Prostate segmentation in mr images
497 using ensemble deep convolutional neural networks. Paper presented at: IEEE 14th
498 International Symposium on Biomedical Imaging (ISBI) - From Nano to Macro; 2017
499 Apr 18-21, 2017; Melbourne, AUSTRALIA.
- b160** 16 He B, Xiao D, Hu Q, Jia F. Automatic Magnetic Resonance Image Prostate Segmenta-
501 tion Based on Adaptive Feature Learning Probability Boosting Tree Initialization and
502 CNN-ASM Refinement. *IEEE Access*. 2018;6:2005-2015.
- b173** 17 Wang B, Lei Y, Tian S, et al. Deeply supervised 3D fully convolutional networks with
504 group dilated convolution for automatic MRI prostate segmentation. *Medical Physics*.
505 2019;46(4):1707-1718.
- b186** 18 Shen DG, Herskovits EH, Davatzikos C. An adaptive-focus statistical shape model for
507 segmentation and shape modeling of 3-D brain structures. *IEEE Transactions on Medical
508 Imaging*. 2001;20(4):257-270.
- b199** 19 Seim H, Kainmueller D, Heller M, Lamecker H, Zachow S, Hege H-C. Automatic Segmen-
510 tation of the Pelvic Bones from CT Data Based on a Statistical Shape Model. *VCBM*.
511 2008;8:93-100.
- b202** 20 Zhang X, Tian J, Deng K, Wu Y, Li X. Automatic Liver Segmentation Using a Statis-
513 tical Shape Model With Optimal Surface Detection. *IEEE Transactions on Biomedical
514 Engineering*. 2010;57(10):2622-2626.
- b215** 21 Alba X, Pereanez M, Hoogendoorn C, et al. An Algorithm for the Segmentation of
516 Highly Abnormal Hearts Using a Generic Statistical Shape Model. *IEEE Transactions
517 on Medical Imaging*. 2016;35(3):845-859.
- b228** 22 Lüthi M, Blanc R, Albrecht T, et al. Stalismo-A framework for PCA based statistical
519 models. *The Insight Journal*. 2012;2012:1-18.

- b23**₀ 23 Szegedy C, Liu W, Jia Y, et al. Going Deeper with Convolutions. Paper presented at: IEEE Conference on Computer Vision and Pattern Recognition (CVPR); 2015 Jun 07-12, 2015; Boston, MA.
- b24**₃ 24 Ronneberger O, Fischer P, Brox T. U-Net: Convolutional Networks for Biomedical Image Segmentation. Paper presented at: 18th International Conference on Medical Image Computing and Computer-Assisted Intervention (MICCAI); 2015 Oct 05-09, 2015; Munich, GERMANY.
- b25**₇ 25 Jaderberg M, Simonyan K, Zisserman A. Spatial transformer networks. *Advances in neural information processing systems*. 2015;28:2017-2025.
- b26**₉ 26 Balakrishnan G, Zhao A, Sabuncu MR, Gutttag J, Dalca AV. Voxelmorph: a learning framework for deformable medical image registration. *IEEE transactions on medical imaging*. 2019;38(8):1788-1800.
- b27**₂ 27 Litjens G, Toth R, van de Ven W, et al. Evaluation of prostate segmentation algorithms for MRI: The PROMISE12 challenge. *Medical Image Analysis*. 2014;18(2):359-373.
- b28**₄ 28 Bloch N, Madabhushi A, Huisman H, et al. NCI-ISBI 2013 challenge: automated segmentation of prostate structures. *The Cancer Imaging Archive*. 2015;370:6.
- b29**₆ 29 Heimann T, Meinzer H-P. Statistical shape models for 3D medical image segmentation: A review. *Medical Image Analysis*. 2009;13(4):543-563.
- b30**₈ 30 Ou Y, Doshi J, Erus G, Davatzikos C. Multi-atlas segmentation of the prostate: A zooming process with robust registration and atlas selection. *Medical Image Computing and Computer Assisted Intervention (MICCAI) Grand Challenge: Prostate MR Image Segmentation*. 2012;7:1-7.
- b31**₂ 31 Gao Q, Rueckert D, Edwards P. An automatic multi-atlas based prostate segmentation using local appearance-specific atlases and patch-based voxel weighting. *MICCAI Grand Challenge: Prostate MR Image Segmentation*. 2012;2012.
- b32**₅ 32 Maan B, van der Heijden F. Prostate MR image segmentation using 3D active appearance models. *MICCAI Grand Challenge: Prostate MR Image Segmentation*. 2012;2012.
-

- b337** 33 Vincent G, Guillard G, Bowes M. Fully automatic segmentation of the prostate using active appearance models. *MICCAI Grand Challenge: Prostate MR Image Segmentation*. 2012;2012:2.
548
549
- b340** 34 Karimi D, Samei G, Kesch C, Nir G, Salcudean SE. Prostate segmentation in MRI using a convolutional neural network architecture and training strategy based on statistical shape models. *International Journal of Computer Assisted Radiology and Surgery*. 2018;13(8):1211-1219.
551
552
553
- b354** 35 Milletari F, Navab N, Ahmadi S-A, Ieee. V-Net: Fully Convolutional Neural Networks for Volumetric Medical Image Segmentation. Paper presented at: 4th IEEE International Conference on 3D Vision (3DV); 2016 Oct 25-28, 2016; Stanford Univ, Stanford, CA.
555
556
- b367** 36 Toth R, Madabhushi A. Deformable landmark-free active appearance models: application to segmentation of multi-institutional prostate MRI data. *MICCAI Grand Challenge: Prostate MR Image Segmentation*. 2012;2012.
558
559
- b370** 37 Tian Z, Liu L, Zhang Z, Fei B. PSNet: prostate segmentation on MRI based on a convolutional neural network. *Journal of Medical Imaging*. 2018;5(2).
561
- b382** 38 Jia H, Xia Y, Song Y, Cai W, Fulham M, Feng DD. Atlas registration and ensemble deep convolutional neural network-based prostate segmentation using magnetic resonance imaging. *Neurocomputing*. 2018;275:1358-1369.
563
564
- b395** 39 Qin C, Cao Z, Fan S, et al. An oral and maxillofacial navigation system for implant placement with automatic identification of fiducial points. *International journal of computer assisted radiology and surgery*. 2019;14(2):281-289.
566
567
- b408** 40 Tu P, Qin C, Guo Y, et al. Ultrasound image guided and mixed reality-based surgical system with real-time soft tissue deformation computing for robotic cervical pedicle screw placement. *IEEE Transactions on Biomedical Engineering*. 2022. doi:10.1109/TBME.2022.3150952.
569
570
571